

Towards ‘good’ seismic data: beyond alias interpolation and filtering in the complex wavelet domain

Iga Pawelec* and Paul Sava*

**Colorado School of Mines,*

1500 Illinois St,

Golden, CO 80401

(March 14, 2023)

CWP-1018

Running head: **CWT reconstruction and filtering**

ABSTRACT

Seismic data can provide a wealth of information about subsurface. The process of obtaining interpretable volumes is involved and intricate, but it starts with the raw data acquired in the field. ‘Good’ raw data should enable the use of state of the art noise suppression tools and thus allow for high resolution subsurface imaging. The key to good data is the ability to capture wavefields without gaps and aliasing which in most situations is impossible or prohibitively expensive. As a result, data are often regularly sampled, but contain gaps in areas of restricted access and suffer from aliasing artifacts. Both of these challenges can be tackled after transforming data into a domain in which their key characteristics can be easily identified and leveraged for guiding wavefield reconstruction. We find that a discrete complex wavelet transform is an optimal domain for representing intricate land seismic wavefields. Taking advantage of the multiscale decomposition and seismic data sparsity in the complex wavelet domain, we develop a multiscale soft thresholding algorithm (MIST) that uses low frequency, low wavenumber information to guide the reconstruction of higher frequen-

cies and wavenumbers. Our approach is successful in interpolation beyond aliasing and in infilling large gaps, but its effectiveness is sampling-dependent, requiring access to non-aliased wavelet coefficients at the deepest possible decomposition level. We also demonstrate the filtering outcomes possible to achieve for non-aliased data. Exploiting the spatio-temporal and frequency-wavenumber localization capability of complex wavelet transform, we develop a velocity filter that allows to target noise of particular phase velocity or range of velocities that is also restricted in time and space. We demonstrate the filter by removing airblast energy from a land seismic record. Our filter preserves features underlying noise and does not affect any signals outside of the predicted airblast trajectory.

INTRODUCTION

Active seismic data are acquired to provide detailed subsurface information such as structural or stratigraphic images, depositional sequences, material and reservoir properties (wave propagation velocities, anisotropy, density, porosity, fluid saturation), or time-lapse differences in these properties. The confidence in inferences made from the acquired seismic volumes depends on the data quality and uncertainties associated with processing and inversion. But what does it mean to have ‘good data’? The answer may not be obvious. An important ingredient of data quality is trace density (Ourabah et al., 2015; Yanchak et al., 2018; Alkatheeri et al., 2020). Dense acquisitions are characterized by high fold which is directly related to the random incoherent noise suppression by stacking (Schimmel and Paulssen, 1997). However, for most onshore acquisitions it is the coherent, slowly propagating waves that contaminate the desired data and degrade the migrated volumes (Regone et al., 2015; Manning et al., 2019; Ourabah et al., 2019; Stork, 2020). Examples of such noise include surface and guided waves, airblast, and scattering noise. These types of coherent noise are best addressed when recorded non-aliased.

Non-aliased recordings of complex land wavefields can be difficult to achieve in practice. If one follows the traditional regular sampling theorem (Shannon, 1948; Jerri, 1977) or its m -D extension (Petersen and Middleton, 1962), the sampling interval required is dictated by the slowest apparent velocity of the observed wavefield and the highest frequency present in the slow moveout features. For some acquisition settings, this criterion may call for regular sampling intervals of less than 2 m, which is prohibitively expensive for most acquisition campaigns. Furthermore, land acquisitions frequently have to be planned around existing infrastructure and natural obstacles, leading to gaps in the acquired seismic volumes.

A possible solution to these problems is compressive sensing (CS) acquisition that uses ran-

domized sampling and sparse data representation in some domain to reconstruct the non-aliased wavefield as a post-acquisition step (Li et al., 2012; Mosher et al., 2017; Jiang et al., 2018, 2019). However, that solution is not always a viable option. One problem is that the compressive sensing approach cannot be applied to the already acquired regular data, as most seismic data are collected on regular or approximately regular grids. When aliasing occurs, such sampling solutions do not lend themselves to data reconstruction following compressive sensing rules because aliases masquerade as real signals, and make aliased data appear sparse. Any sizable gaps in data are also a problem regardless of sampling scheme (Trad et al., 2005). Large concentrations of missing traces introduce illumination gaps and ultimately may prevent one from achieving a desired imaging objective. A 5D interpolation (Trad, 2009) is helpful when reciprocal information about the gap interior is available (i.e., skipped shot locations infilled from receiver data when possible). However, such information is not always present or of sufficient quality, and the often high dynamic range of land seismic data introduces further complications.

Though at the first glance it may not seem like the problems of regular aliased data and significant data gaps are related, simple solutions can help to address them both. Spitz (1991) shows that non-aliased low frequency information can be used to guide the interpolation of higher frequency aliased events by designing appropriate prediction error filters (PEFs) in the F-X domain. Gülünay (2003) demonstrates that FK domain interpolation operator designed to manipulate low non-aliased frequencies can guide the unraveling of aliased data. However, a common problem with these and other Fourier domain approaches (Duijndam et al., 1999; Zwartjes and Sacchi, 2007; Naghizadeh and Innanen, 2011; Naghizadeh, 2012; Gao et al., 2013) is that they assume stationary signals. When the wavefield considerably varies in amplitude and frequency as a function of time and space, methods assuming signal stationarity struggle. To overcome this problem, Liu and Fomel (2011) introduce adaptive prediction error filters, obtaining the nonstationary coefficients by

solving global regularized least squares problem. Guitton and Claerbout (2010) develop a pyramid transform to estimate a single PEF that accounts for non-stationarity. Another solution is to take advantage of local transforms, e.g., the approach described by Naghizadeh and Sacchi (2010) that uses non-aliased curvelet scales for interpolation. The curvelet transform Candès et al. (2006) is an oriented and localized generalization of the Fourier transform. While it provides sparse representations of wavefields (Candès and Demanet, 2005), it is a highly redundant transformation, with a scale-dependent redundancy level. A less redundant alternative to curvelets is the discrete complex wavelet transform which we elect to use for data reconstruction and filtering.

The discrete complex wavelet transform (\mathbb{C} WT) was developed to overcome certain shortcomings of its real-valued counterpart that made wavelets sub-optimal for image processing. Unlike the real wavelet transform, \mathbb{C} WT offers near shift invariance, the ability to distinguish between dip directions, and an intuitive interpretation for detecting signal singularities (Selesnick et al., 2005). While the transform implementation necessitates redundancy, its degree depends only on the dimensionality of decomposed objects and is 2^m for m -dimensional signals, meaning that the number of \mathbb{C} WT coefficients representing data is $N \times 2^m$. Furthermore, the transform has an efficient implementation via filter bank with the computational complexity of $\mathcal{O}(N)$ which is better than the $\mathcal{O}(N \log N)$ complexity of the Fast Fourier transform. Combined, these features make the \mathbb{C} WT an attractive domain for performing data interpolation.

Since \mathbb{C} WT naturally decomposes signals into different octave bands from the Fourier domain, it can easily adapt the philosophy of using non-aliased (low frequency, low wavenumber) scales to guide the data reconstruction in large gaps and for regularly missing aliased traces. We describe how to adapt an iterative soft thresholding algorithm (Daubechies et al., 2004) for a multiscale reconstruction that follows \mathbb{C} WT decomposition levels and provide examples that illustrate its effectiveness. In particular, we show that multiscale iterative soft thresholding (MIST) succeeds in

interpolation beyond aliasing and in infilling large gaps, yielding reconstructed wavefields that can be subsequently processed without suffering the consequences of inadequate sampling.

We also demonstrate how the CWT can be used to accomplish the next task in the quest for the good quality data, namely, wavefield denoising. Non-aliased wavefields make it easier to separate signal and noise by their characteristics in the transform domain. CWT is localized in time, space, frequency, and wavenumber, enabling straightforward definition of velocity filters. Different types of noise such as surface waves, airblast, guided waves, or first arrivals that have near-linear moveout or range of moveouts can be suppressed with a well-defined velocity filter. Such filters are commonly applied in the Fourier domain but because of the stationarity assumption and the lack of time-space localization, an FK filter targeting specific slope erases all instances of events with similar slopes, thus risking the loss of valuable diffractions or reflection tails. We can avoid this shortcoming by defining a velocity filter in the CWT domain. We explain how to determine which scales and orientations of the CWT should be used for filtering and how to incorporate spatial moveout information for best filtering outcomes.

COMPLEX WAVELET RECONSTRUCTION AND FILTERING

In geophysics we frequently deal with highly non-stationary signals. It was the need to study the minute changes in amplitude, phase, frequency and shape of seismic reflection signals as a function of propagation time that motivated Morlet et al. (1982) to use wavelets as an analysis tool to characterize wave scattering regimes for different wavelengths and media types. Although non-stationary signals can be analyzed with the short time Fourier transform (STFT), wavelets are an attractive alternative because they provide a multiresolution decomposition of signals. In STFT, an analysis window is selected at the start and kept the same for all times and frequencies. The time-frequency

resolution, which is the ability to distinguish between two discrete spikes in time domain and two pure frequency sinusoids in the frequency domain, is therefore fixed and bounded by the Heisenberg uncertainty (Gabor, 1946):

$$\Delta t \Delta f \geq \frac{1}{2}, \quad (1)$$

with Δt and Δf indicating time and frequency resolution, respectively. Keeping the resolution fixed over the entire time-frequency plane imposes limitations on how well specific signal features can be localized in time or in frequency. The idea behind the wavelet transforms is to vary Δt and Δf such that the time resolution becomes arbitrarily good at high frequencies while the frequency resolution becomes arbitrarily good at low frequencies (Rioul and Vetterli, 1991), thus obtaining the multiresolution representations of signals. This is achieved by keeping the relative bandwidths constant, most commonly using 2:1 scaling that yields octave bandwidths (Kingsbury, 1999). Naturally, wavelet decompositions are still subject to the uncertainty principle from equation 1, but by selecting long analysis windows for low frequency and short windows for high frequency content, our ability to distinguish time-frequency signal characteristics is significantly improved.

The multiresolution signal analysis is not restricted to 1D cases. A discrete 2D wavelet transform is used in image processing problems such as denoising, restoration, compression, and segmentation. However, using a critically sampled real wavelet transform in image processing can be challenging because of its strong shift dependence and the lack of sufficient directional selectivity. Critical sampling refers to the transform implementation via filter bank with analysis (decomposition) filters whose number equals the downsampling factor. Shift variance implies that the energy concentration of wavelet coefficients at each decomposition scale depends on time or space shifts of the input signal, which can lead to erratic and inconsistent processing outcomes. The limited directional sensitivity means that it is not possible to distinguish the direction of dipping features,

for instance, in 2D it is not possible to tell the difference between $\pm 45^\circ$. These shortcomings led to the development of discrete complex wavelet transform (CWT) that is near shift invariant and capable of distinguishing dip directions (Kingsbury, 1999, 2001; Selesnick et al., 2005).

Complex wavelet transform

By introducing approximately analytic complex wavelets (whose support is finite, preventing them from being exactly analytic), the CWT is able to mimic desirable properties of the Fourier transform, providing complex coefficients whose phases depend on signal shifts almost linearly while magnitudes are largely shift invariant (Kingsbury, 2001; Selesnick et al., 2005). An exactly The complex wavelet is defined as

$$\psi_C(t) = \psi_r(t) + i\psi_i(t), \quad (2)$$

with real-valued functions $\psi_r(t)$ and $\psi_i(t)$ that are odd and even, respectively. Wavelets act as highpass filters. To achieve a lowpass at the lowest decomposition level, a complex scaling function is also introduced:

$$\phi_C(t) = \phi_r(t) + i\phi_i(t), \quad (3)$$

with similar properties to the complex wavelet. The transform is implemented via a dual-tree filter bank, as described by Kingsbury (2001) and Selesnick et al. (2005). The m -D wavelet can be obtained by taking a tensor product of wavelets along all dimensions. Directional selectivity is achieved because CWT uses analytic wavelets, allowing to distinguish between positive and negative wavenumbers. If we use a seismic convention for Fourier spectrum representation of real-valued signals, the frequency axis contains only positive frequencies, while wavenumbers can be either positive or negative. A specific scale and orientation in CWT corresponds to an octave band representing frequency and either positive or negative wavenumbers. Such support allows for 6 distinct

orientations in 2D and 28 orientations in 3D transform.

Due to the favorable properties described above, complex wavelets found many interesting applications such as volume registration where one seeks to detect and compensate for motion between images or volumes (Chen and Kingsbury, 2012), video denoising (Selesnick and Li, 2003) and a wide array of image processing problems, where \mathbb{C} WT outperforms their real-valued transform alternative (Kingsbury, 1999; Miller and Kingsbury, 2008; Chitchian et al., 2009; Raj and Venkateswarlu, 2012).

Although we often display geophysical data as if they are images, we have to remember that they represent physical quantities as a function of time, or space, or both, rather than the scaled light intensity or color coding for pixels. As a consequence, the range of possible coefficient values for transformed geophysical data differs from that of image data. Moreover, data sampling rate and the number of samples available in each sampling direction impose inherent limitations on what processing outcomes can be achieved with the aid of \mathbb{C} WT because they control the number of possible decomposition levels and central frequencies and wavenumbers corresponding to \mathbb{C} WT scales and orientations. Understanding how geophysical data, and seismic data in particular, are represented in the complex wavelet domain is the key to optimizing data reconstruction and to designing effective filters.

Rotational variance

One potential problem with \mathbb{C} WT is that certain orientations correspond to central frequencies and wavenumbers that are further from the origin than others. The orientations formed by combining lowpass and highpass filters have central frequencies that are approximately $\sqrt{1.8}$ closer to the origin than orientations formed by combining highpass filters (Kingsbury, 2006). This has interesting

implications for data reconstruction, as illustrated next.

Consider a circularly symmetric object such as in Figure 1. For such an image, the transform orientations should represent angles and since a circle has the same amount of all angles, the coefficient energy distribution should be uniform among all orientations. However, due to center frequency shift, that is not the case. To understand how this affects reconstruction and assess the effect of rotational variance on the reconstruction quality, we conduct a numerical experiment. First, we remove a portion of the data in a shape of circular sector with a 6° angle. Starting with a gap centered at 0° azimuth, we run a sparsity-promoting reconstruction. We repeat that process for gaps oriented along all azimuths with a 1° interval. Each reconstruction is quantified by the normalized root mean squared error (NRMSE) and plotted against gap azimuth. The higher the NRMSE, the less favorable a particular gap orientation is from the reconstruction point of view and vice-versa. Example reconstructions for 0° , 45° and 90° are shown in the top row of Figure 1, and the middle row shows the difference (magnified by 10) between fully sampled object and its reconstruction. Note that reconstruction error is the biggest for 45° and related to amplitude, while phase is reconstructed accurately. The bottom plot in Figure 1 highlights the good orientations with green stars and poor orientations with red crosses. As expected, 45° , 135° , 225° and 315° are poor because they represent gaps aligned with orientations for which two high-pass filters were used to achieve the decomposition. Interestingly, when the gaps are nearly aligned with the sampling axes (in this case, x or y), reconstructions quickly shift from good to bad or the other way around. We are unsure about the cause of such behavior but suspect that it might be related to representing a circular sector with square pixels with limited number of samples.

Multiscale CWT reconstruction

As a consequence of rotational variance and unequal coefficient energy distribution among orientations, we can expect certain wavefield features to be more challenging to reconstruct than others, simply because they are represented by weaker coefficients than other features of a similar amplitude but different slope in the data domain. One way to address that problem in the reconstruction algorithm is to minimize the effect of unequal coefficient distribution among scales and orientations by introducing scale- and orientation-dependent thresholds within an iterative soft thresholding algorithm. In (manuscript under revision), we describe the threshold estimation process that takes advantage of the available data to obtain parameters σ_n and $\sigma_w(s, \gamma)$ that are then used to estimate the thresholds as $\lambda_{s, \gamma} = \frac{\sigma_n^2}{\sigma_w(s, \gamma)}$. We refer to that Chapter for further details.

Let \mathbf{d} be the acquired data, \mathbf{S} the sampling operator projecting the acquired data on the desired regular fine grid, Ψ the forward CWT, and α the complex wavelet domain representation of the fully sampled wavefield. The data recovery problem can then be formulated as a mixed norm optimization problem:

$$\min_{\alpha} \|\mathbf{d} - \Psi^H \mathbf{S}^H \alpha\|_2^2 + \lambda \|\alpha\|_1, \quad (4)$$

with the regularization parameter λ . The solution can be found by iterative soft thresholding algorithm (Chambolle et al., 1998; Figueiredo and Nowak, 2003; Beck and Teboulle, 2009) whose general step is

$$\alpha_{k+1} = \mathcal{T}_{\lambda t} \left(\alpha_k - 2t \mathbf{S} \Psi (\Psi^H \mathbf{S}^H \alpha_k - \mathbf{d}) \right), \quad (5)$$

where t denotes the step size. We define the complex thresholding operator for scale- and orientation-dependent thresholds $\lambda_{s, \gamma}$. Let $\alpha_k = r_k e^{j\theta_k}$. Then

$$\mathcal{T}_{\lambda_{s,\gamma}}(\alpha_k) = \mathcal{T}_{\lambda_{s,\gamma}}(r_k)e^{j\theta_k} = \begin{cases} (r_k + \lambda_{s,\gamma})e^{j\theta_k} & \text{for } r_k \geq \lambda_{s,\gamma} \\ 0 & \text{for } r_k < \lambda_{s,\gamma} \end{cases}, \quad (6)$$

Rather than threshold all scales at the same time, we modify the algorithm by introducing a multiscale approach. A pseudo code summarizing our strategy is described in Algorithm 1. We start by estimating the initial thresholds $\lambda_{s,\gamma}$ from data projected onto the target grid, \mathbf{Sd} . The initial complex wavelet domain approximation of the fully sampled wavefield is obtained as $\alpha_0 = \Psi\mathbf{P}\mathbf{Sd}$, where \mathbf{P} denotes a smoothing operator along the spatial dimensions. The purpose of this low resolution initial guess is to mitigate potential influence of data gaps at the deepest complex wavelet decomposition level. Starting with these deep level coefficients, we apply thresholding at the active scale and set all of the higher frequency, higher wavenumber scales to 0. When no further improvement can be achieved from a given scale, we move to a finer level and recompute the thresholds from an object that has original data traces where available and the lower scale approximation elsewhere. By doing so, we minimize the impact that the gaps presence has on the distribution and energy level of complex wavelet coefficients. The final reconstruction is achieved either when we reach the desired relative data residual or the maximum number of iterations.

A threshold re-computation step is important for reconstructing regularly missing traces. When the CWT is computed, each data decomposition level means a data decimation by a factor of 2 along all axes. For example, the level 1 decomposition coefficients are computed from data downsampled by a factor of 2, level 2 means downsampling by a factor of 4, level 3 by a factor of 8, etc. If data have enough spatial and temporal samples to allow for complex wavelet decomposition with at least one scale not suffering from aliasing effects, we can use it for beyond aliasing data reconstructions. However, for scales corrupted by aliasing effects, the original thresholds are sub-optimal and likely

to reinforce a form of periodicity inherent in sampling, ultimately leading to poor reconstructions. In such situations, one may try to apply a constant velocity NMO correction to data prior attempting the reconstruction so as to lessen the aliasing impact by making dipping events less steep (Yu et al., 2017).

A similar reasoning can be applied when one is concerned with reconstructing data within large gaps. The deepest decomposition level is the least affected by the gap presence, allowing us to gradually rebuild the missing information. When the gap is large enough to impact wavelet coefficients at all scales, the gap effect on the coarsest scale can be lessened by smoothing data along the spatial dimension. The degree of smoothing should be chosen based on the gap size and maximum decomposition level so as to eliminate wavelet coefficient discontinuity that gap introduces.

©WT velocity filter design

©WT could also be used for data filtering, which is not a new idea. Yu and Whitcombe (2008) and Yu et al. (2017) discuss the use of ©WT as a dip filter, pointing out that the success of filtering depends on the ability to separate the signal and noise in the transform domain and suggesting the use of constant velocity NMO correction in order to improve that separation. The filter is then defined to target specific scales and orientations in the transform domain and removes the undesirable energy by setting all targeted coefficients to 0. However, knowing which scales and orientations to target can be difficult and non-intuitive, particularly when the commonly assumed image processing jargon uses angles to describe orientations.

To help with geophysical intuition behind complex wavelet scales and orientations, consider displaying wavelet coefficients on their idealized Fourier support. As explained earlier, scales and orientations represent Fourier octave bands whose central frequencies depend on data spatial and

Algorithm 1 MIST

Inputs: $\mathbf{d}, \mathbf{S}, \sigma_n, \text{maxlevel}, \text{maxit}, \epsilon, \text{tol}$ **Initialize:** $\lambda_{s,\gamma} \leftarrow f(\mathbf{S}\mathbf{d}, \sigma_n)$

Thresholds from available data

 $\alpha_0 \leftarrow \Psi\mathbf{P}\mathbf{S}\mathbf{d}$

Low resolution estimate

 $s_k \leftarrow \text{maxlevel}$

Maximum CWT decomposition level

 $\text{rez}_0 \leftarrow \|\mathbf{d}\|_2^2$

Initial data residual

 $k \leftarrow 0$ **while** $\frac{\text{rez}_k}{\text{rez}_0} > \epsilon$ **and** $k < \text{maxit}$ **do** **if** $s \geq s_k$ **then** $\alpha_{k+1}(s, \gamma) \leftarrow \mathcal{T}_{\lambda_{s,\gamma}}(\alpha_k - \mathbf{S}\Psi(\Psi^H\mathbf{S}^H\alpha_k - \mathbf{d}))$ **else** $\alpha_{k+1}(s, \gamma) \leftarrow 0$ **end if** $\text{rez}_k \leftarrow \|\mathbf{d} - \Psi^H\mathbf{S}^H\alpha_k\|_2^2$ **if** $\frac{\text{rez}_k - \text{rez}_{k-1}}{\text{rez}_k} \leq \text{tol}$ **then** **continue** **else** $s_k \leftarrow s_k - 1$ $\lambda_{s,\gamma} \leftarrow f(\mathbf{S}\mathbf{d}, \sigma_n, \alpha_k)$

Use current data approximation inside gaps and original data where available to get new thresholds

end if $k \leftarrow k + 1$ **end while****Output:** $\mathbf{m} \leftarrow \Phi^H\alpha_k$

temporal sampling. Figure 2 shows the type of display we are advocating for. The horizontal axis represents wavenumbers while the vertical axis represents frequencies. Solid black lines mark the boundaries between scales and orientations. By identifying the box location in the $f - k$ coordinates, we are able to assign frequencies and wavenumbers to a particular scale and orientation.

Assigning the $f - k$ bands to CWT scales and orientations means that we can also map phase velocities. Figure 3 shows how such mapping can be done. Note that $x - t$ sampling defines spatial and temporal Nyquist, directly affecting whether specific phase velocities are mapped to the same or different CWT orientation. Both panels are generated assuming the spatial sampling of 2 m, but temporal sampling is selected as 1 ms in Figure 3a and 4 ms in Figure 3b. For a 1 ms case, the velocity of 1800 m/s falls into the orientation that is typically associated with 45° , but for a 4 ms sampling it is assigned to 15° orientation. Therefore, trying to associate seismic events with CWT orientations based purely on the angular interpretation of orientations may be misleading. Plots like the ones shown in Figure 3 are easy to generate for arbitrary samplings, decomposition levels, and velocities and are a valuable tool to aid in selecting scales and orientations for filtering or in adjusting data sampling that would achieve orientation separation between specific events.

Before we move on to defining a complex wavelet domain filter, we need to discuss one other aspect of CWT : the spatio-temporal localization. Coefficient magnitudes and phases in Figure 2 form patterns that distinctly resemble seismic data. This is because CWT is also localized in time and space. To find $t - x$ coordinates corresponding to a particular coefficient, one only needs to know the original data coordinates and the decomposition level. Spatial and temporal sampling at scale s is $dx_s = dx_0/2^s$ and $dt_s = dt_0/2^s$, with dx_0 and dt_0 representing the data sampling. Therefore, to map a $t - x$ slope between decomposition levels, one only needs to appropriately scale the coordinates.

3D seismic data $\mathbf{d}(x, y, t)$ can be represented by their 3D CWT :

$$\alpha(\mathbf{x}, \mathbf{y}, \mathbf{t}, \gamma, \mathbf{s}) = \Phi \mathbf{d}(\mathbf{x}, \mathbf{y}, \mathbf{t}), \quad (7)$$

with orientation γ and scale \mathbf{s} . One can define a binary filter in the transform domain as (Yu et al., 2017):

$$\mathbf{Q}(\mathbf{x}, \mathbf{y}, \mathbf{t}, \gamma, \mathbf{s}) = \begin{cases} 1, & \text{if } \mathbf{Q} \in \text{selected } (\mathbf{x}', \mathbf{y}', \mathbf{t}', \gamma', \mathbf{s}') \\ 0, & \text{otherwise} \end{cases} \quad (8)$$

Therefore, filtering can be viewed as an application of binary masks to complex wavelet coefficients. Yu et al. (2017) suggest to define filter coefficients over scales and orientations only. However, such an approach disregards spatio-temporal localization of complex wavelets, hindering filtering outcomes for events that are not sufficiently distinguished from useful signals in scales and orientations only. We propose to define a filtering mask that is time- and space-dependent for each scale and orientation:

$$\mathbf{Q}(\gamma, \mathbf{s}) = f(\mathbf{x}, \mathbf{y}, \mathbf{t}), \quad (9)$$

with the mask values that can take any values from $[0, 1]$ interval. This allows for introducing moveout-based filtering masks that have a more gradual transition between pass and reject bands, mitigating edge effects. We illustrate this idea in the following section.

EXAMPLES

In this section, we demonstrate the practical uses for our multiscale reconstruction and complex wavelet domain velocity filtering. We start with interpolation beyond aliasing example showcasing wavefield recovery from regularly missing traces. Next, we show how the multiscale approach

handles infilling large gaps and what can be done to improve the reconstruction outcome. Finally, we present the CWT velocity filter design to suppress the airblast from a land seismic record.

Regular data interpolation beyond aliasing

Regular coarse sampling that results in spatially aliased data is a common problem. Figure 4a shows a fully sampled synthetic wavefield with a wide range of data amplitudes and event orientations. We use symmetric logarithmic color normalization from *matplotlib* (Hunter, 2007) for wavefield display to better highlight weaker signals. To test the capability of MIST for reconstructing regularly missing aliased data, we only keep every fourth trace from Figure 4a leading to coarsely sampled wavefield in Figure 4b. FK spectra for both wavefields are shown in Figures 4c and 4d.

To evaluate the performance of MIST, we compare it with a sparsity promoting basis pursuit. The goal of this comparison is to judge whether the sparsity assumption alone would be sufficient to recover the missing data. Figure 5 summarizes the reconstruction outcomes for basis pursuit and MIST. Since the initial threshold estimation plays an important role for MIST, we show a reconstruction for thresholds obtained from the available coarsely sampled data and another reconstruction where the initial thresholds are estimated based on the wavefield recovered from the previous MIST reconstruction.

Figure 5a shows that sparsity alone is not sufficient to infill gaps in regularly decimated data. The wavefield reconstructed following the basis pursuit suffers from sampling artifacts and has severe problems in recovering accurate amplitudes. MIST does markedly better, maintaining structural consistency in most places. Data differences obtained by subtracting reconstructed data from a fully sampled wavefield in Figure 4a reveal that the reconstruction error is the most significant for steeply dipping events as well as some near-horizontal features and becomes smaller if we re-

run the reconstruction with thresholds recomputed from a previous reconstruction. Note that the spectrum from Figure 5h still has a remnant sampling imprint that dominates the basis pursuit reconstruction. However, that imprint is much smaller than for the original data, allowing the recomputed thresholds to handle these spectral artifacts.

Infilling large gaps

In land acquisition, we frequently face access restrictions preventing the placement of sources and/or receivers at desired locations. To simulate such a scenario and evaluate how data reconstruction handles gaps, we introduce a 16 traces-long gap (marked with a black box in Figure 6a). Its size in the physical domain is 160 m, and the dominant wavelength corresponding to the strongest event is approximately 450 m.

Similarly to the previous experiment, we compare MIST reconstruction against the basis pursuit solution. Figures 6b and 6c show the reconstructions in the context of the entire wavefield, while Figures 6e and 6f zoom-in on details inside the gap. Basis pursuit reconstruction struggles to recover reflection amplitudes and moveouts, with fidelity getting progressively worse going from gap edges to its middle. The coherent but weak energy before reflections is barely represented. In contrast, MIST reconstruction recovers reflections with accurate moveout but amplitudes are slightly weaker than those of the original data. Weak energy before and after reflections is also reconstructed, but it is the moveouts of those events that are of particular interest. Comparing the zoomed-in reconstruction from Figure 6f to the reference data in Figure 6d, we can notice that the reconstruction created events that do not exist in reference data (for example, a near-infinite velocity feature around 2.47 s). This happens because interpolation is incapable of creating new information - we can only use what we have in clever ways to fill in the missing data. By removing a portion of data, we risk permanent

information loss. Data surrounding the gap do not provide sufficient information about some events - especially those that are not continuous through the gap. Therefore, one has to be careful about spurious events that might be created by an interpolation.

Airblast removal

The airblast or air wave is frequently observed on land seismic records. Traveling with the speed of sound in the air (usually around 330 - 340 m/s), the airblast is a broadband signal that obscures valuable reflection data and provides no information about subsurface. It is desirable to have this signal removed with as little effect on the underlying data as possible. Rather than using a surgical mute, we demonstrate the use of a $t - x - f - k$ -localized complex wavelet domain velocity filter to accomplish this task.

The filtering is done by multiplying complex wavelet coefficients with the corresponding filter masks whose values can vary continuously between 0 and 1. Because the moveout of an airblast can be predicted with a known source location and air wave speed, we are able to define appropriate masks as shown in Figure 8. We use a chart from Figure 3a to pinpoint CWT orientations that should contain the majority of the energy we seek to remove. Figure 7 shows an airblast contaminated land record, its filtered version, and the difference between raw and filtered data. To avoid signal distortions at near offsets (-90,90) m, we can exclude them from the filtering either setting the corresponding CWT filter coefficients to 1 or by re-injecting near offset traces after filtering. Note that the filter is effective: the energy corresponding to the airblast is largely removed and the underlying signals are preserved. Due to the spatio-temporal filter localization, none of the steeply dipping events that do not follow the predicted airblast moveout are affected. This result is promising for a wide breadth of filtering applications for noise that can be separated in $t - x - f - k$ space,

such as surface and guided waves, first breaks, or vibroseis-generated chimney noise (Bagaini et al., 2014).

DISCUSSION

We demonstrate that complex wavelets can be successfully applied to solve a variety of geophysical problems involving data reconstruction and filtering. The key to successful processing outcomes is in the recording parameters of signals: array length and recording time affect the number of possible decomposition levels of CWT and effectively control transform resolution, while spatial and temporal sampling intervals define Nyquist wavenumber and frequency. Since CWT decomposes signals into octave bands, data sampling affects feature separability.

We find that a multiscale iterative soft thresholding is effective in restoring aliased signals. However, this technique assumes that there is a scale for which the aliasing effects are minimal or non-existent. When aliasing has severe imprint on the coefficients at the deepest possible decomposition level, the reconstruction is likely to fail. A partial solution for overcoming this limitation is to use a constant velocity NMO prior to data reconstruction to lessen the degree of aliasing (Yu et al., 2017).

Another important factor to consider is the data dimensionality. In this paper, we consider 2D examples for reconstruction and filtering, but our techniques can be extended to higher dimensions. Working in higher dimensions, in particular when both source and receiver axes are available, can have implications for infilling large gaps. Although it is still true that no data reconstruction technique can create new information, access to a volume with multiple illuminations increases chances that the features which should be present inside a gap are captured somewhere in the data volume. Thus, we expect higher-dimensional reconstructions to yield better gap infills.

For the reasons mentioned above, CWT reconstruction and filtering outcomes are data dependent. It is important to consider data sampling to establish what can be reasonably achieved. With favorable data parameters, CWT velocity filters are effective at suppressing coherent noise that can be separated in $t - x - f - k$ space because we can define the spatial and temporal origin of signals to be suppressed as well as their moveout or range of moveouts. Examples include surface waves, guided waves, and first breaks. One can also define a narrow time-space cone to address chimney noise generated by vibroseis at near offsets (Bagaini et al., 2014).

CONCLUSIONS

Seismic data processing, imaging, and inversion outcomes are the best when we have access to non-aliased data that do not have significant gaps. The complex wavelet domain can help in achieving that if the acquired data do not already have these desirable attributes. The multiresolution character of wavelets naturally predisposes them to address sampling challenges. We show that by leveraging non-aliased information from the deepest decomposition level, our multiresolution iterative soft thresholding is successful both in reconstruction beyond aliasing and in large gap reconstruction.

One of the advantages of non-aliased data is the significantly improved ability for noise suppression. Separating signal and noise is contingent upon achieving the best possible noise separation in the transform domain. Because CWT is localized in $t - x - f - k$ space, it allows one to design filters based on velocities as well as expected $t - x$ moveouts. The advantage of such design is demonstrated with airblast removal: we show that CWT velocity filter is effective in removing airblast energy and does not affect any signals outside of expected noise trajectory.

REFERENCES

- Alkatheeri, T., G. Cambois, M. Mahgoub, G. Nyein, P. Vasilyev, I. Mihaljevic, and M. Doheim, 2020, Processing ultra-high density 3D seismic surveys: an Abu Dhabi case study: Abu Dhabi International Petroleum Exhibition & Conference, SPE, 1–10.
- Bagaini, C., M. Laycock, C. Readman, E. Coste, and C. Anderson, 2014, Seismo-acoustic characterization of a seismic vibrator: Society of Exploration Geophysicists International Exposition and 84th Annual Meeting SEG 2014, 3877–3881.
- Beck, A., and M. Teboulle, 2009, A fast iterative shrinkage-thresholding algorithm for linear inverse problems: *SIAM Journal on Imaging Sciences*, **2**, 183–202.
- Candès, E., L. Demanet, D. Donoho, and L. Ying, 2006, Fast discrete curvelet transforms: *Multi-scale Modeling & Simulation*, **5**, 861–899.
- Candès, E. J., and L. Demanet, 2005, The curvelet representation of wave propagators is optimally sparse: *Communications on Pure and Applied Mathematics*, **58**, 1472–1528.
- Chambolle, A., R. De Vore, Nam-Yong Lee, and B. Lucier, 1998, Nonlinear wavelet image processing: variational problems, compression, and noise removal through wavelet shrinkage: *IEEE Transactions on Image Processing*, **7**, 319–335.
- Chen, H., and N. Kingsbury, 2012, Efficient registration of nonrigid 3-D bodies: *IEEE Transactions on Image Processing*, **21**, 262–272.
- Chitchian, S., M. A. Fiddy, and N. M. Fried, 2009, Denoising during optical coherence tomography of the prostate nerves via wavelet shrinkage using dual-tree complex wavelet transform: *Journal of Biomedical Optics*, **14**, 014031.
- Daubechies, I., M. Defrise, and C. De Mol, 2004, An iterative thresholding algorithm for linear inverse problems with a sparsity constraint: *Communications on Pure and Applied Mathematics*, **57**, 1413–1457.

- Duijndam, A. J. W., M. A. Schonewille, and C. O. H. Hindriks, 1999, Reconstruction of band-limited signals, irregularly sampled along one spatial direction: *Geophysics*, **64**, 524–538.
- Figueiredo, M., and R. Nowak, 2003, An EM algorithm for wavelet-based image restoration: *IEEE Transactions on Image Processing*, **12**, 906–916.
- Gabor, D., 1946, A theory of communication. Part 1: The analysis of information.: *Journal of the Institution of Electrical Engineers-part III: radio and communication engineering*, **93**, 429–441.
- Gao, J., A. Stanton, M. Naghizadeh, M. D. Sacchi, and X. Chen, 2013, Convergence improvement and noise attenuation considerations for beyond alias projection onto convex sets reconstruction: *Geophysical Prospecting*, **61**, 138–151.
- Guitton, A., and J. Claerbout, 2010, An algorithm for interpolation in the pyramid domain: *Geophysical Prospecting*, **58**, 965–976.
- Gülünaý, N., 2003, Seismic trace interpolation in the Fourier transform domain: *Geophysics*, **68**, 355–369.
- Hunter, J. D., 2007, Matplotlib: A 2D Graphics Environment: *Computing in Science & Engineering*, **9**, 90–95.
- Jerri, A., 1977, The Shannon sampling theorem—Its various extensions and applications: A tutorial review: *Proceedings of the IEEE*, **65**, 1565–1596.
- Jiang, T., P. Eick, Y. Jiang, T. Li, H. Hao, W. Chu, R. Holt, D. Blymyer, K. Koster, and D. Enns, 2019, Compressive sensing seismic processing tests on a high density blended land data set: *SEG Technical Program Expanded Abstracts 2019*, Society of Exploration Geophysicists, 4505–4509.
- Jiang, T., Y. Jiang, D. Clark, R. Gray, and D. Brost, 2018, A compressive seismic field trial and reconstruction test using regular indexing: *SEG Technical Program Expanded Abstracts*, Society of Exploration Geophysicists, 86–90.
- Kingsbury, N., 1999, Image processing with complex wavelets: *Philosophical Transactions of the*

- Royal Society of London. Series A: Mathematical, Physical and Engineering Sciences, **357**, 2543–2560.
- , 2001, Complex wavelets for shift invariant analysis and filtering of signals: Applied and Computational Harmonic Analysis, **10**, 234–253.
- , 2006, Rotation-invariant local feature matching with complex wavelets: European Signal Processing Conference.
- Li, C., C. C. Mosher, and S. T. Kaplan, 2012, Interpolated compressive sensing for seismic data reconstruction: SEG Technical Program Expanded Abstracts 2012, Society of Exploration Geophysicists, 1–6.
- Liu, Y., and S. Fomel, 2011, Seismic data interpolation beyond aliasing using regularized nonstationary autoregression: Geophysics, **76**, V69–V77.
- Manning, T., D. Ablyazina, and J. Quigley, 2019, The nimble node - million-channel land recording systems have arrived: Leading Edge, **38**, 706–714.
- Miller, M., and N. Kingsbury, 2008, Image denoising using derotated complex wavelet coefficients: IEEE Transactions on Image Processing, **17**, 1500–1511.
- Morlet, J., G. Arens, E. Fourgeau, and D. Glard, 1982, Wave propagation and sampling theory—Part I: Complex signal and scattering in multilayered media: Geophysics, **47**, 203–221.
- Mosher, C. C., C. Li, F. D. Janiszewski, L. S. Williams, T. C. Carey, and Y. Ji, 2017, Operational deployment of compressive sensing systems for seismic data acquisition: The Leading Edge, **36**, 661–669.
- Naghizadeh, M., 2012, Seismic data interpolation and denoising in the frequency-wavenumber domain: Geophysics, **77**.
- Naghizadeh, M., and K. A. Innanen, 2011, Seismic data interpolation using a fast generalized Fourier transform: Geophysics, **76**, V1–V10.

- Naghizadeh, M., and M. D. Sacchi, 2010, Beyond alias hierarchical scale curvelet interpolation of regularly and irregularly sampled seismic data: *Geophysics*, **75**, WB189–WB202.
- Ourabah, A., A. Crosby, C. Brooks, E. Manning, K. Lythgoe, D. Ablyazina, V. Zhuzhel, E. Holst, and T. Knutsen, 2019, A comparative field trial of a new nimble node and cabled systems in a desert environment: 81st EAGE Conference and Exhibition 2019, European Association of Geoscientists & Engineers, 1–5.
- Ourabah, A., J. Keggin, C. Brooks, D. Ellis, and J. Etgen*, 2015, Seismic acquisition, what really matters?: SEG Technical Program Expanded Abstracts 2015, Society of Exploration Geophysicists, 6–11.
- Petersen, D. P., and D. Middleton, 1962, Sampling and reconstruction of wave-number-limited functions in N-dimensional euclidean spaces: *Information and Control*, **5**, 279–323.
- Raj, V. N. P., and T. Venkateswarlu, 2012, Denoising of medical images using dual tree complex wavelet transform: *Procedia Technology*, **4**, 238–244.
- Regone, C., M. Fry, and J. Etgen, 2015, Dense sources vs. dense receivers in the presence of coherent noise: A land modeling study: SEG Technical Program Expanded Abstracts, **34**, 12–16.
- Rioul, O., and M. Vetterli, 1991, Wavelets and signal processing: *IEEE Signal Processing Magazine*, **8**, 14–38.
- Schimmel, M., and H. Paulssen, 1997, Noise reduction and detection of weak, coherent signals through phase-weighted stacks: *Geophysical Journal International*, **130**, 497–505.
- Selesnick, I., R. Baraniuk, and N. Kingsbury, 2005, The dual-tree complex wavelet transform: *IEEE Signal Processing Magazine*, **22**, 123–151.
- Selesnick, I. W., and K. Y. Li, 2003, Video denoising using 2D and 3D dual-tree complex wavelet transforms: *Wavelets: Applications in Signal and Image Processing X*, 607.
- Shannon, C. E., 1948, A mathematical theory of communication: *Bell System Technical Journal*,

27, 379–423.

Spitz, S., 1991, Seismic trace interpolation in the F-X domain: *Geophysics*, **56**, 785–794.

Stork, C., 2020, How does the thin near surface of the earth produce 10–100 times more noise on land seismic data than on marine data?: *First Break*, **38**, 67–75.

Trad, D., 2009, Five-dimensional interpolation: Recovering from acquisition constraints: *Geophysics*, **74**, V123–V132.

Trad, D., J. Deere, and S. Cheadle, 2005, Challenges for land data interpolation: CSEG Annual Convention, Expanded Abstracts, 309–311.

Yanchak, D., D. Monk, and J. Versfelt, 2018, Egypt West Kalabsha 3D broadband ultrahigh density seismic survey: SEG Technical Program Expanded Abstracts 2018, Society of Exploration Geophysicists, 4080–4084.

Yu, Z., R. Abma, J. Etgen, and C. Sullivan, 2017, Attenuation of noise and simultaneous source interference using wavelet denoising: *Geophysics*, **82**, V179–V190.

Yu, Z., and D. Whitcombe, 2008, Seismic noise attenuation using 2D complex wavelet transform: 70th EAGE Conference and Exhibition incorporating SPE EUROPEC 2008, European Association of Geoscientists & Engineers, 2050–2054.

Zwartjes, P. M., and M. D. Sacchi, 2007, Fourier reconstruction of nonuniformly sampled, aliased seismic data: *Geophysics*, **72**, V21–V32.

LIST OF FIGURES

1 Gap orientation sensitivity test. We remove a piece of an arch from the circularly symmetric object, run complex wavelet reconstruction, and repeat the test at multiple angular orientations. The top row shows reconstructions for 0° , 45° , and 90° , respectively, and the middle row shows difference between original and reconstructed object magnified 10x. Each reconstruction is quantified by NRMSE and plotted against gap azimuth (bottom). Dashed lines show primary angular sensitivity directions for a 2D CWT. The most favorable reconstructions are indicated by green stars while the least favorable are marked with red crosses.

2 (a) Magnitude and (b) phase of complex wavelet coefficients for a land seismic record sampled at 2 m and 4 ms. The largest coefficients correspond to the high energy events and to the features supported by given scale and orientation (e.g., that fast first arrivals have strong coefficients at 62.5 - 125 Hz, -0.1 - 0.1 1/m, which follows the geophysical intuition). The phase spectrum reveals that high frequency, high wavenumber features do not form many coherent patterns, indicating that these CWT bands primarily support noise.

3 Mapping of different phase velocities to CWT orientations assuming spatial sampling of 2 m and temporal sampling of (a) 1 ms and (b) 4 ms. Note that changing the temporal sampling alters the distribution of phase velocities among CWT scales and orientations which has implications for noise suppression and signal separation.

4 (a) Fully sampled wavefield and (b) wavefield after spatial decimation by a factor of 4. (c) and (d) are the corresponding FK spectra.

5 Reconstructions of aliased wavefield from Figure 4b on a fine grid. (a) Reconstruction by basis pursuit, and (b) and (c) are obtained with MIST using decimated data or reconstructed data as an input. (d)-(e) show the corresponding data differences, while (f)-(h) show the FK spectra.

6 (a) Reference data with a 160m (16 traces) gap marked with the black box and the re-

constructed wavefields using (b) basis pursuit and (c) MIST. (d)-(f) show the gap interior. MIST has better amplitude accuracy, but is sometimes unable to accurately reproduce event moveouts, for example the diffraction tail around 2.47 s and 1200 m visible in (d).

7 Airblast removal in the complex wavelet domain. (a) raw data, (b) after removing the airblast, and (c) data difference. Data are gained and clipped for display. Note that the majority of the airblast energy is removed without affecting other events.

8 Complex wavelet domain filter masks for airblast suppression. Note that we only target the scales and orientations that are the most affected by the airblast energy, leaving others unchanged.

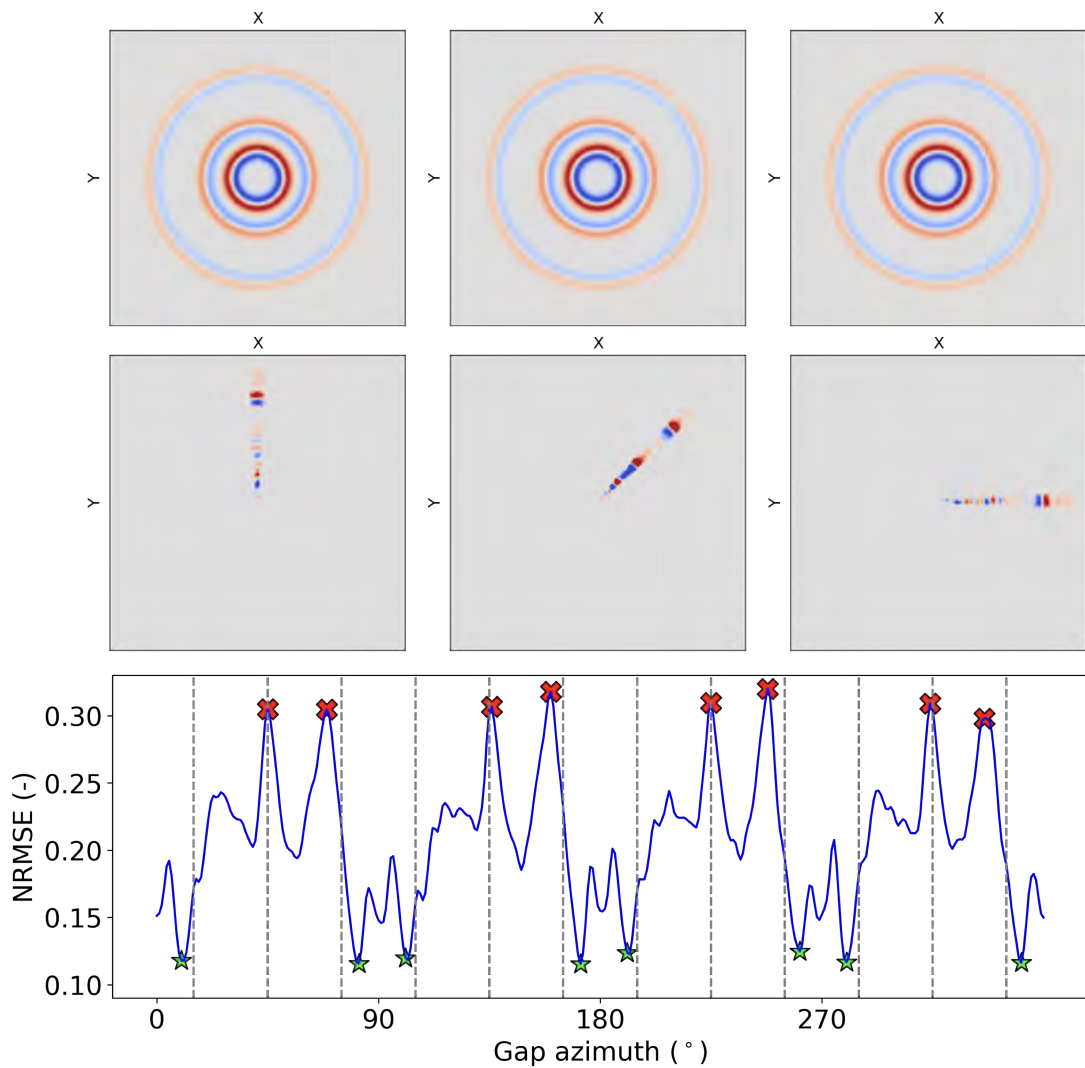


Figure 1: Gap orientation sensitivity test. We remove a piece of an arch from the circularly symmetric object, run complex wavelet reconstruction, and repeat the test at multiple angular orientations. The top row shows reconstructions for 0° , 45° , and 90° , respectively, and the middle row shows difference between original and reconstructed object magnified 10x. Each reconstruction is quantified by NRMSE and plotted against gap azimuth (bottom). Dashed lines show primary angular sensitivity directions for a 2D CWT. The most favorable reconstructions are indicated by green stars while the least favorable are marked with red crosses.

– CWP-1018

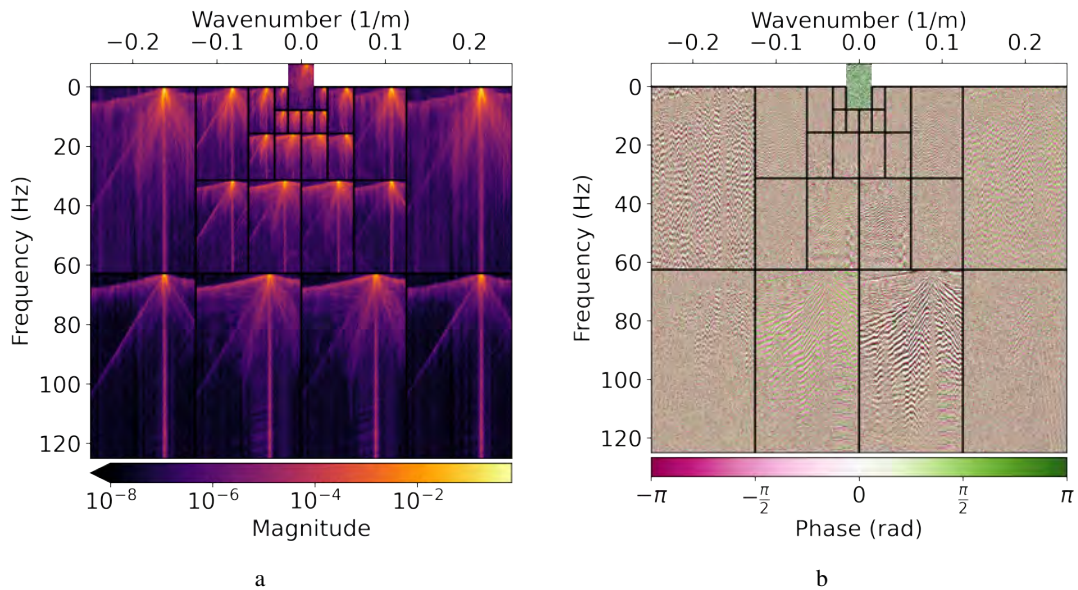


Figure 2: (a) Magnitude and (b) phase of complex wavelet coefficients for a land seismic record sampled at 2 m and 4 ms. The largest coefficients correspond to the high energy events and to the features supported by given scale and orientation (e.g., that fast first arrivals have strong coefficients at 62.5 - 125 Hz, -0.1 - 0.1 1/m, which follows the geophysical intuition). The phase spectrum reveals that high frequency, high wavenumber features do not form many coherent patterns, indicating that these CWT bands primarily support noise.

– CWP-1018

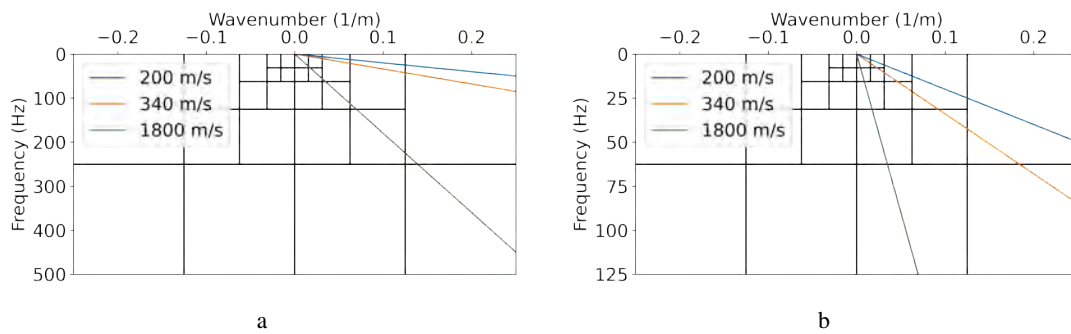


Figure 3: Mapping of different phase velocities to CWT orientations assuming spatial sampling of 2 m and temporal sampling of (a) 1 ms and (b) 4 ms. Note that changing the temporal sampling alters the distribution of phase velocities among CWT scales and orientations which has implications for noise suppression and signal separation.

– CWP-1018

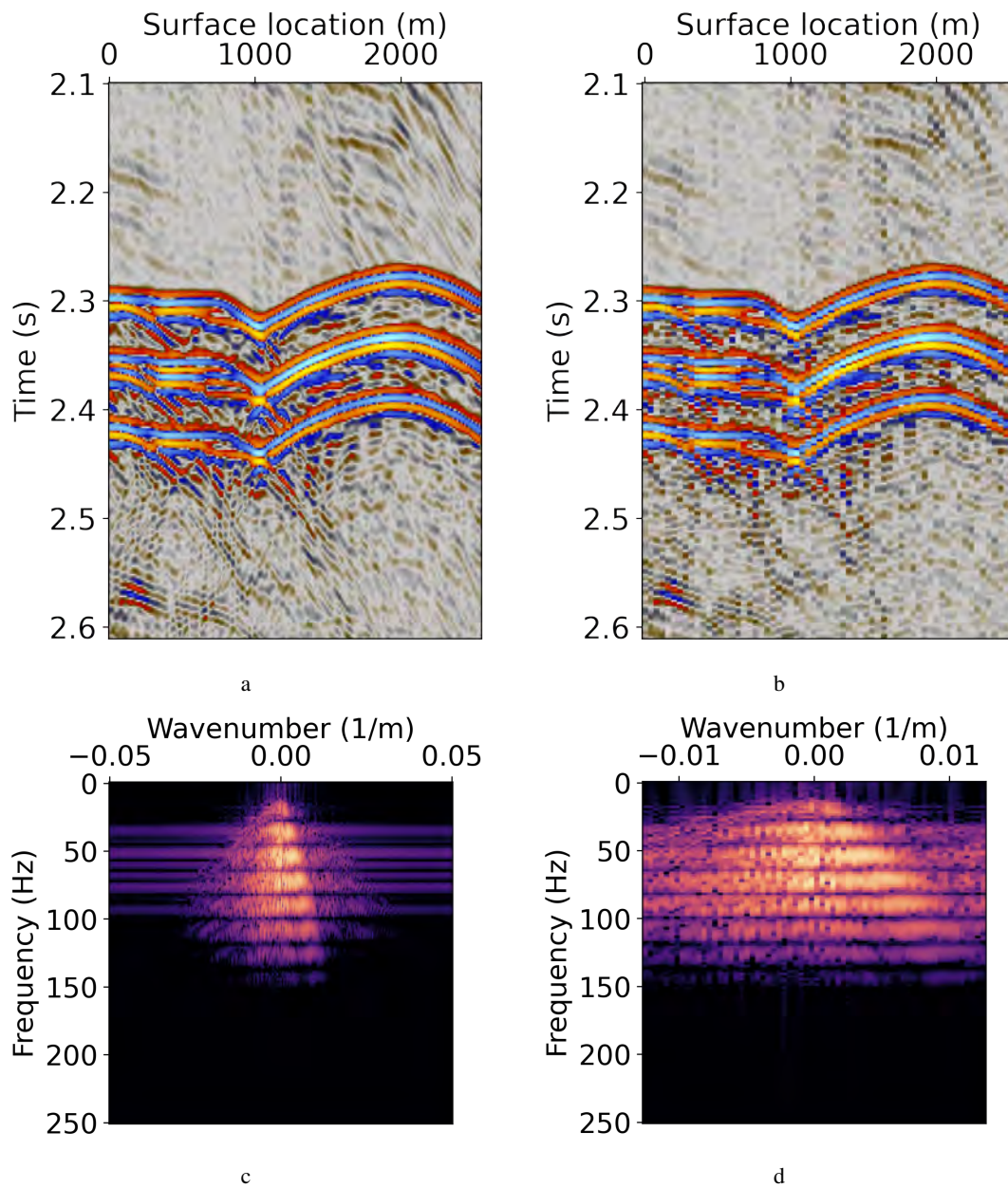


Figure 4: (a) Fully sampled wavefield and (b) wavefield after spatial decimation by a factor of 4. (c) and (d) are the corresponding FK spectra.

– CWP-1018

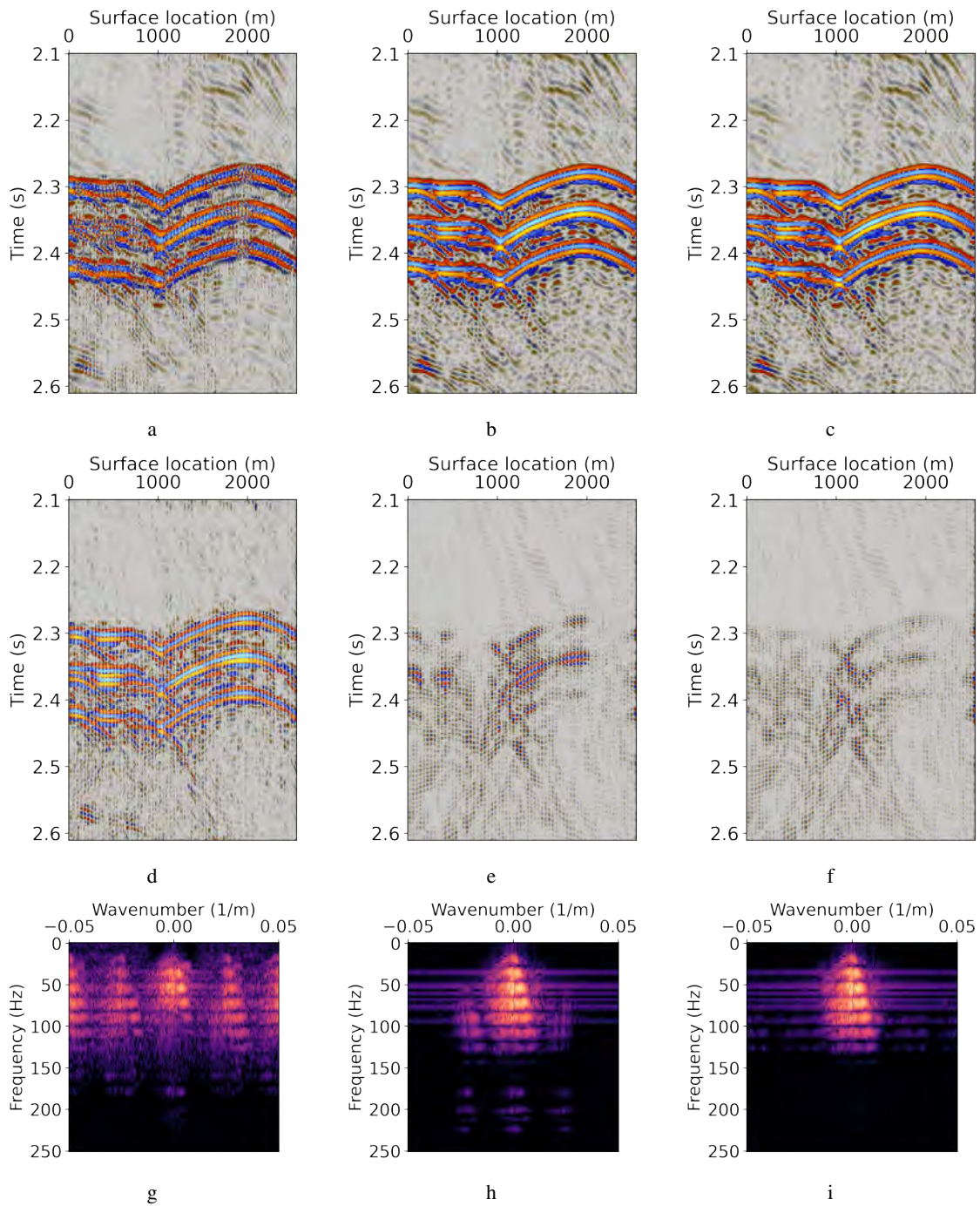


Figure 5: Reconstructions of aliased wavefield from Figure 4b on a fine grid. (a) Reconstruction by basis pursuit, and (b) and (c) are obtained with MIST using decimated data or reconstructed data as an input. (d)-(e) show the corresponding data differences, while (f)-(h) show the FK spectra.

– CWP-1018

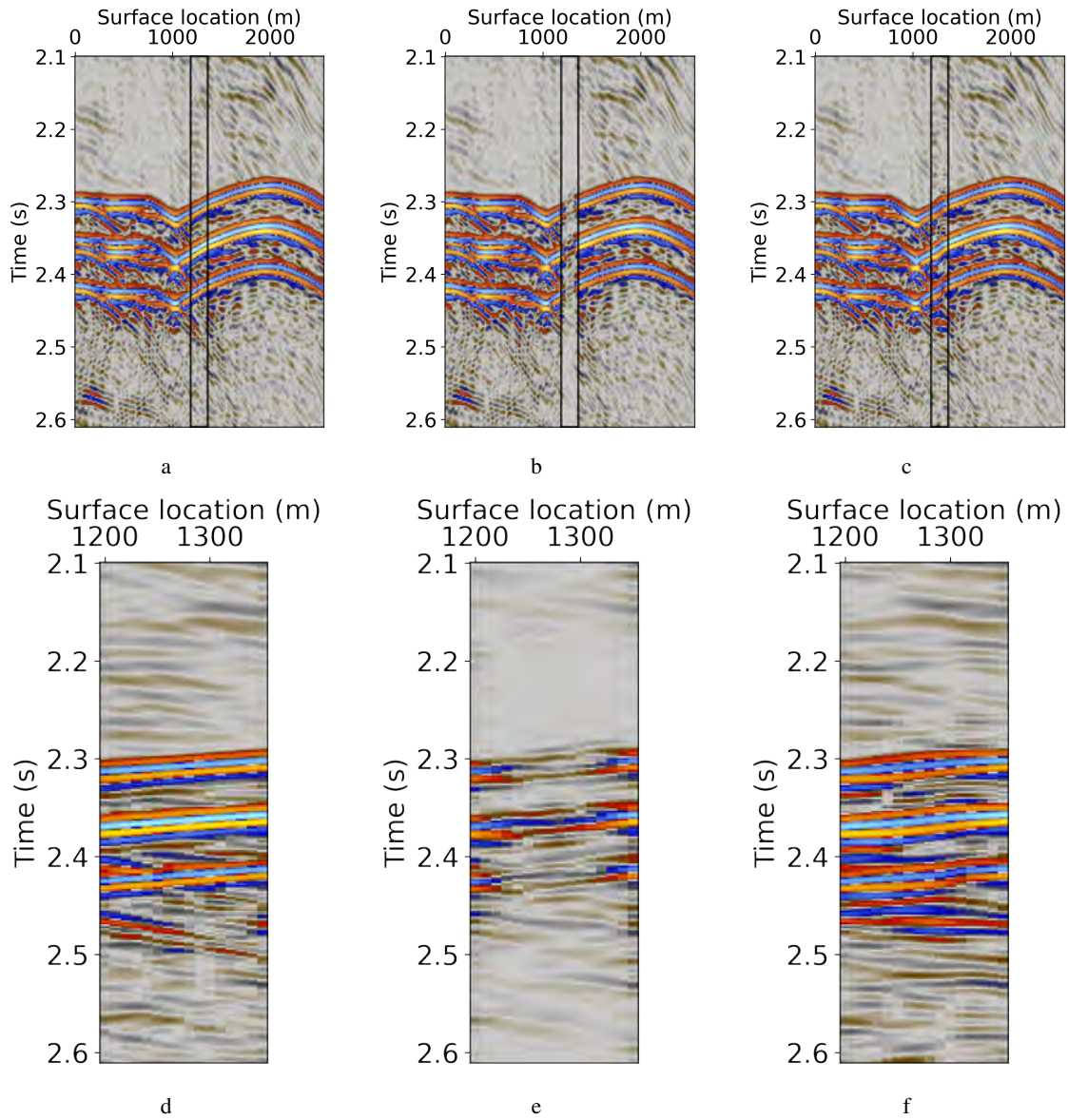


Figure 6: (a) Reference data with a 160m (16 traces) gap marked with the black box and the reconstructed wavefields using (b) basis pursuit and (c) MIST. (d)-(f) show the gap interior. MIST has better amplitude accuracy, but is sometimes unable to accurately reproduce event moveouts, for example the diffraction tail around 2.47 s and 1200 m visible in (d).

– CWP-1018

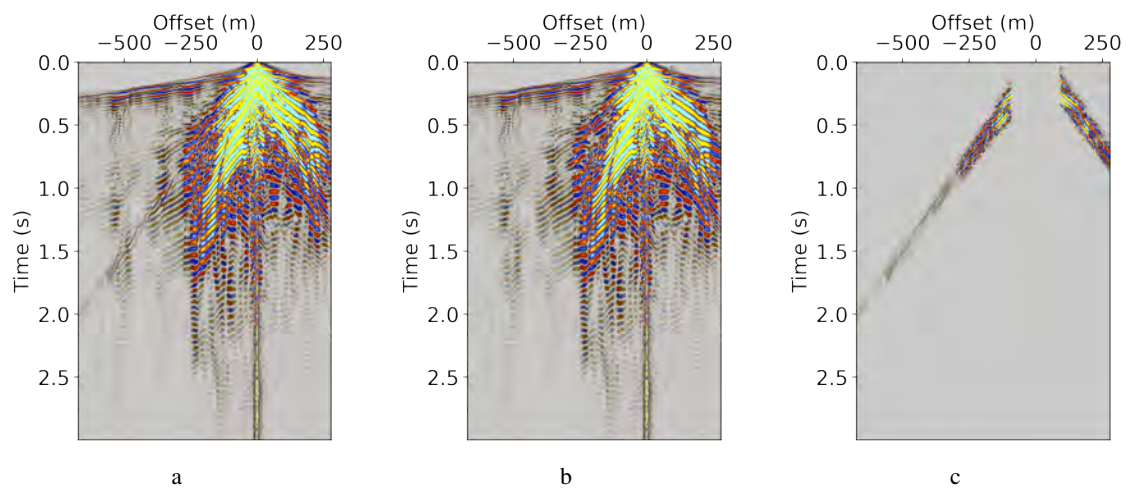


Figure 7: Airblast removal in the complex wavelet domain. (a) raw data, (b) after removing the airblast, and (c) data difference. Data are gained and clipped for display. Note that the majority of the airblast energy is removed without affecting other events.

– **CWP-1018**

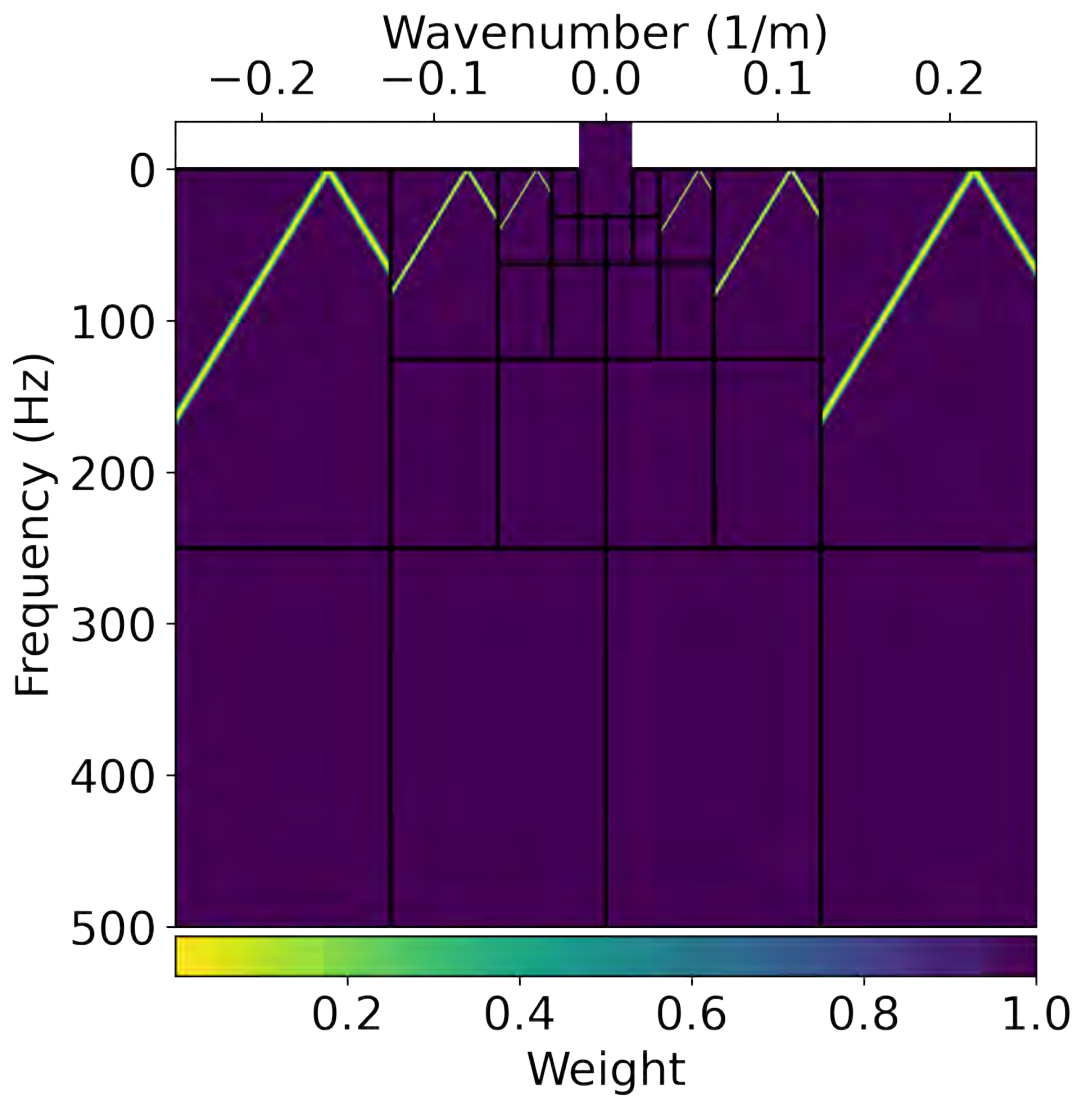


Figure 8: Complex wavelet domain filter masks for airblast suppression. Note that we only target the scales and orientations that are the most affected by the airblast energy, leaving others unchanged.
 – CWP-1018